1   **Tailoring interfacial properties of 3D-printed continuous natural fiber reinforced**

2   **polypropylene composites through parameter optimization using machine**

3   **learning methods**

4   Ruijun Cai[a], Wei Wen[b], Kui Wang[a]*, Yong Peng[a], Said Ahzi[c], Francisco Chinesta[d]

5   [a] Key Laboratory of Traffic Safety on Track of Ministry of Education, School of Traffic

6   & Transportation Engineering, Central South University, Changsha 410075, China

7   [b] Department of Engineering, Lancaster University, Lancaster, LA1 4YR, UK

8   [c] ICUBE Laboratory-CNRS, University of Strasbourg, Strasbourg 67000, France

9   [d] ESI Chair, PIMM, Arts et Métiers Institute of Technology, Paris 75013, France

10   * Corresponding author e-mail address: kui.wang@csu.edu.cn

11   **Abstract**

12   3D-printed continuous ramie fiber reinforced polypropylene composites

13   (CRFRPP) are expected to ensure good mechanical properties while meeting the

14   requirements of environmental friendliness and sustainability. To promote the wide

15   industrial application of CRFRPP, this work investigated the effects of printing

16   parameters (extrusion flow rate, printing temperature, layer thickness and printing

17   speed) on the interfacial properties of CRFRPP. The interlayer and intralayer interfacial

18   properties of CRFRPP with different printing parameters were studied using the design

19   of experiment approach. Machine learning methods and response surface methodology

20   prediction were also carried out based on the experimental results to bridge the printing

21   parameters and interfacial properties. According to the prediction results, the printing

22   parameters were optimized to improve the production efficiency while ensuring the

23   desired interfacial performance. At last, the bending tests were conducted to investigate

24   how the difference in interfacial properties can be translated to the mechanical

25   performance. The results found that printed specimens with weak interfacial strength

26   suffered interlaminar delamination failure when subjected to bending loads, greatly

27   weakening the mechanical properties of the composites.

28

29   **Keywords**: Additive manufacturing; Interfacial properties; Continuous natural fiber;

30   Machine learning; Polypropylene-based composites

31   **1 Introduction**

32   Additive manufacturing (AM), also known as 3D printing, is a promising

33   manufacturing technology for quickly and cost-effectively fabricating objects with

34   complicated structures [1]. Material extrusion-based additive manufacturing (ME-AM)

35   is a widely used AM method that fabricated 3D parts by selectively laying extruded

36   semi-molten thermoplastic materials. ME-AM has attracted increasing attention due to

37   its advantages of simple process, cost-saving, high forming efficiency and multi-

38   material flexibility [2]. However, some challenges, such as voids in the microstructure

39   and poor interfacial interaction, impact negatively the mechanical properties of printed

40   parts thus limiting the industrial application of ME-AM products [3]. Driven by these

41   challenges and applications, polymer-based particles, short fiber and continuous fiber

42   reinforced composites have been intensively investigated to improve the properties of

the printed parts. Among these composites, continuous fiber reinforced composites

usually outperform particles and short fiber reinforced composites in terms of

mechanical performance [3-5]. The current literature mainly focused on 3D-printed

continuous synthetic fibers reinforced composites [6, 7]. However, the extensive use of

non-biodegradable synthetic fiber materials would affect negatively the environment

[8]. Taking into account the needs of environmental friendliness and sustainable

development, natural fibers were suggested as the replacement for synthetic fibers [8,

9].

Continuous natural fiber reinforced composite prepared by ME-AM is still a

young field of research with limited works in the literature available. Matsuzaki et al.

[10] fabricated jute reinforced polylactic acid (PLA)-based composites by in-situ

impregnation 3D printing method and investigated their tensile properties. It was found

that the tensile modulus and strength of the continuous jute reinforced PLA printed

specimen increased by 157% and 134%, respectively, compared with those of the 3D-

printed neat PLA specimens. Le Duigou et al. [11] investigated the tensile properties of

ME-AM fabricated continuous flax fiber reinforced PLA composites. The results

showed that the longitudinal tensile modulus and strength of continuous flax fiber

reinforced PLA composites were improved by a factor of 4.5. In another work of Le

Duigou et al. [12], the mechanical properties of 3D-printed continuous flax/PLA

biocomposites were demonstrated to be very sensitive to the printing parameters such

as layer thickness and interfilament distance. Cheng et al. [6] investigated the effects of

64 printing parameters on interfacial and tensile mechanical properties of continuous ramie

65 fiber reinforced PLA fabricated by ME-AM. The results indicated that the interfacial

66 and tensile mechanical properties of the printed ramie/PLA composites increased as

67 increasing printing temperature and decreasing layer thickness as well as printing speed.

68   It can be seen that PLA as the matrix of continuous natural fiber reinforced

69 composites is getting more attention due to its facile processability and biodegradability.

70 However, PLA was severely limited by its relatively low toughness and poor heat

71 resistance [13, 14]. In recent years, PP has emerged as a new 3D printing material due

72 to its heat stability and excellent balance between toughness and rigidness [15].

73 Moreover, PP had superior remanufacturing capacity among various commercially

74 available 3D printing materials [16]. Therefore, 3D-printed continuous natural fiber

75 reinforced PP composites have promising potential to be environment-friendly and

76 sustainable composites with good mechanical properties.

77   As previously stated, the mechanical behaviors of 3D-printed continuous fiber

78 reinforced composites highly depended on the printing parameters. In the available

79 studies, the effects of process parameters on the mechanical properties of 3D-printed

80 continuous natural fiber reinforced composites were mainly studied experimentally.

81 However, the experimental methods are time-consuming and costly when considering

82 many parameters and their interactions. Although finite element and theoretical

83 modeling could also be applied to study properties of material and structure, their

84 inherent physical assumptions and high computational costs make them challenging to

85   analyze 3D-printed composites with complex microstructures [17-21]. In addition,

86   when interrelated variables are presented in a nonlinear pattern, it is difficult to reveal

87   their relationships using traditional methods [20, 22]. The application of data-driven

88   methods, such as machine learning (ML), may provide effective solutions for the above

89   issues. In fact, ML method has been applied to AM with promising results in recent

90   years [20, 22-28].

91   In this work, continuous ramie fiber reinforced PP composites (CRFRPP) were

92   prepared by in-situ impregnation 3D printing. Interfacial (interlayer and intralayer)

93   properties of CRFRPP were investigated as they may impact significantly on the

94   mechanical properties of 3D-printed composites [29-34]. Effects of printing parameters

95   such as extrusion flow rate, printing temperature, layer thickness and printing speed on

96   the interfacial properties of CRFRPP were studied. Box-Behnken design (BBD) and

97   factorial design methods were combined to design experiments with the consideration

98   of reflecting the interaction among parameters as much as possible. Response surface

99   methodology (RSM) was applied to predict interlayer and intralayer adhesion

100   properties of CRFRPP with different printing parameters. In addition, two ML

101   algorithms, random forest (RF) and artificial neural network (ANN) were also applied

102   to build prediction models of interfacial properties. The performance of the above

103   methods was evaluated. Parameters were optimized based on the prediction results

104   given by the prediction model with the best performance. At last, the bending tests were

105   conducted to investigate how the difference in interfacial properties can be translated

106   to the mechanical performance.

107   **2 Experiments and modeling**

108   **2.1 Materials and processing**

109   In this work, commercial talc (12 wt.%) filled and ethylene-propylene-diene-

110   monomer (EPDM) (20 wt.%) toughened commercial PP-based composite,

111   PP/EPDM/talc (grade 7510, Sabic, Saudi Arabia), was selected to be the matrix for

112   CRFRPP. Continuous ramie fiber (Hunan Huasheng Dongting Ramie Textile co., ltd,

113   Hunan, China) was selected to be the reinforcement for CRFRPP in this study. This

114   ramie yarn was twisted (400 turn/meter) with a linear density of 36 Nm/2R. Nm is an

115   indirect yarn count system. The length of yarn in meters of one gram of yarn or the

116   length of yarn in kilometers of one kilogram of yarn is called new metric count (Nm).

117   2R means that the number of strands plied together in the yarn is 2.

118   The as-received granular PP/EPDM/talc material was first dried in an oven at

119   80 °C for one hour and then extruded using a twin-screw extruder at a final die

120   temperature of 185 °C. The filament was extruded evenly by the extruder, keeping a

121   stable diameter of 1.75 mm. The ramie yarns were also dried in an oven at 80 °C for

122   two hours before the 3D printing process. 3D printer allowing in-situ impregnation

123   (Combot-200, Fibertech, Shanxi, China) with a single 1.3 mm diameter flat-head

124   nozzle was applied to fabricate CRFRPP samples in this work. As shown in Fig.1 (a),

125   during the printing process, PP filament was fed into a liquefier to heat and melt. Then

126   the ramie yarn was impregnated with molten PP in the liquefier and together extruded

127   by the nozzle. Under the action of heat and pressure, adjacent extruded filaments

128   within the layer were bonded and then adjacent layers were bonded. The intralayer

129   and interlayer adhesion strengths were denoted as Intra-Strength and Inter-Strength in

130   this study, respectively, as shown in Fig.1 (b). The extruded filament was deposited in

131   a rectilinear pattern.

132
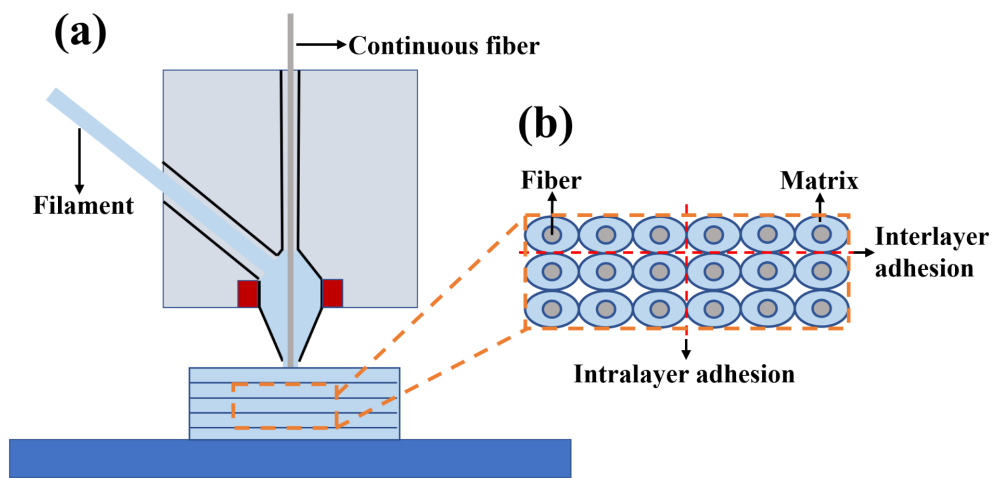
134 **Fig. 1.** Schematic of the (a) in-situ impregnation 3D printing process (b) cross-section

135 of the printed specimen.

136

137 **2.2 Characterization**

138   Four printing parameters that could have great influences on the performance of

139 the printed specimen: extrusion flow rate, printing temperature, layer thickness and

140 printing speed were chosen to study their effects on the interfacial properties of

141 CRFRPP, and each parameter was set at three levels, as shown in Table 1. Note that the

142 extrusion flow rate was the parameter from the slicing software, which meant the

143 extrusion amount of molten resin in unit length, the greater value of it represented the

144 more resin extrusion per unit length. The print line spacing was set at a constant value

145 of 1.0 mm to ensure printed specimens can be successfully printed under all printing

146 parameters combinations in our work. Box-Behnken design (BBD) was used to

147 generate experimental points in this study. For BBD, only tests in the center points were

148 designed to repeat for evaluating the error of experiments [35-37]. In addition, we added

149 12 experimental points to better train and validate ML models for improving prediction

150 accuracy. As a result, each type of test (Inter-strength or Intra-strength test) had 39

151 experimental points and 78 tests were conducted in total.

152

153 **Table 1.** Printing parameters with their codes and levels.

| Printing parameters	Codes	Levels		
		Low level	Center level	High level
Extrusion flow rate (%)	E	50	70	90
Printing temperature (ºC)	T	190	210	230
Layer thickness (mm)	L	0.30	0.45	0.60
Printing speed (mm/min)	V	100	300	500

154

155 The combinations of printing parameters based on the experimental design as well

156 as the experimental results are detailed in section 3.1 (shown in Table 3). According to

157 the experimental design, CRFRPP with different printing parameter combinations were

158   manufactured and their interfacial properties (interlayer and intralayer adhesion

159   properties) were examined. Inspired by these works [33, 38-44] and ASTM D1938

160   standard, interlayer and intralayer adhesion strengths (Inter-Strength and Intra-Strength)

161   of CRFRPP were characterized by the means of methods shown in Fig. 2 using a

162   universal mechanical testing machine (E44, MTS Co., USA). For Inter-Strength

163   characterization, the test specimens with a length of 80 mm and a width of 6 mm were

164   printed as three layers, as shown in Fig. 2 (a). For Intra-Strength characterization, the

165   test specimens with a length of 80 mm and a width of 6 mm were printed as two layers,

166   as shown in Fig. 2 (b). Fig. 2 (c) shows the typical curve for an Inter-Strength

167   measurement (curves for Intra-Strength measurement showed similar trends therefore

168   were not presented). Interlayer and intralayer adhesion forces were obtained from the

169   average of the steady-state region. Then interlayer and intralayer adhesion forces were

170   normalized by width of Inter-Strength test specimen and thickness of Intra-Strength test

171   specimen, respectively.

172
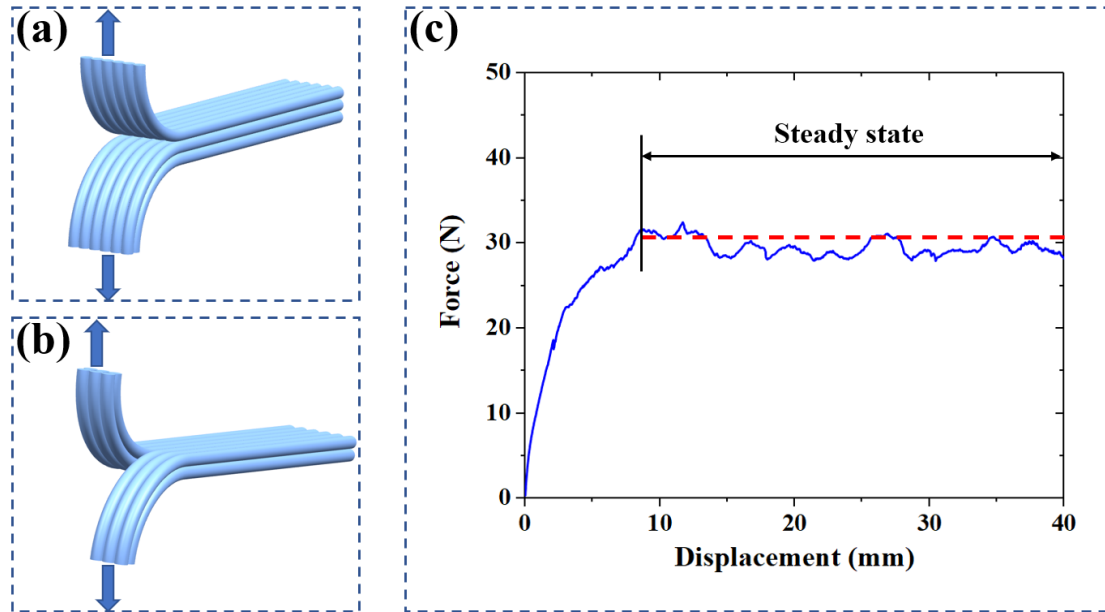
173

174   **Fig. 2.** Schematic of the (a) Inter-Strength and (b) Intra-Strength tests, and (c) typical

175   curve for Inter-Strength measurement.

176

177   To investigate how the interfacial properties influence the mechanical performance

178   of printed specimen, three-point bending tests were carried out using the universal

179   mechanical testing machine. The bending tests were performed with a constant cross-

180   head speed of 3 mm/min and at room temperature according to ISO14125. The bending

181   test specimen was cuboid with dimensions of 90 mm × 6 mm × 6 mm.

182   The morphological properties of the specimens after Inter-Strength and Intra-

183   Strength tests were investigated using an optical microscope (OM) (AO-3M150GS,

184   AOSVI, Shenzhen, China).

185   **2.3 Modeling and evaluation**

186   Three methods, response surface methodology (RSM), random forest (RF) and

187 artificial neural network (ANN), were selected as prediction models. These two ML

188 models were developed using Python (Python Software Foundation). Scikit-learn

189 (scikit-learn package, v0.24.2) [45], an open-source ML library for Python, was used

190 to execute ML algorithms in this study.

191   The dataset used for modeling was built based on the experimental results. Here,

192 the inputs for the models were extrusion flow rate, printing temperature, layer thickness

193 and printing speed. And the outputs were corresponding Inter-Strength and Intra-

194 Strength. The data were randomly divided into training and test datasets in the ratio of

195 9:1, which were used to calibrate the model and validate the results of the training

196 protocol, respectively. For each ML method, hyperparameters were fine-tuned by

197 empirical methods, grid search techniques and references to related literature [23, 46]

198 to maximize model performance. The optimized hyperparameters are shown in Table 2.

199 A brief explanation of the meanings for all hyperparameters mentioned in this study

200 was presented in the Supplementary material.

201

202   **Table 2.** Optimized hyperparameters for machine learning methods in this study.

Method	Method Hyperparameters	Best Parameters
	max_depth	4
RF	min_samples_leaf	1
	min_samples_split	2
	n_estimators	50

	solver	lbfgs
ANN	activation	tanh
	hidden_layer_sizes	(4,3,3,1)
	Max_iter	134

203

204   Four metrics were used to evaluate the accuracy of the prediction. These four

205 metrics were R^2, Mean Absolute Error (MAE), Root Mean Square Error (RMSE) and

206 Median Absolute Error (MedAE). The equations and brief explanations of these metrics

207 were presented in the Supplementary material.

208 **3 Results**

209 **3.1 Experimental results**

210   Table 3 shows the Inter-Strength and Intra-Strength of the CRFRPP under different

211 printing parameters. These results would be used as training and test datasets for ML

212 models. It should be mentioned that Inter-Strength and Intra-Strength derived from the

213 interlayer and intralayer adhesion forces normalized by width of Inter-Strength test

214 specimen and thickness of Intra-Strength test specimen, respectively, so their units are

215 N/cm.

216

217 **Table 3.** Inter-Strength and Intra-Strength of the CRFRPP under different printing

218   parameters.

Tests	Extrusion flow rate (%)	Printing temperature (ºC)	Layer thickness (mm)	Printing speed (mm/min)	Inter-Strength (N/cm)	Intra-Strength (N/cm)
1	50	210	0.45	500	12.56	40.61
2	90	210	0.45	100	29.34	110.38
3	70	230	0.45	100	24.70	113.67
4	70	210	0.6	500	9.69	67.68
5	70	210	0.45	500	14.30	72.79
6	50	230	0.45	300	18.15	68.67
7	90	210	0.45	300	32.34	103.43
8	70	230	0.60	300	20.49	78.04
9	70	190	0.45	100	3.57	34.10
10	70	230	0.45	500	25.31	83.29
11	90	230	0.45	300	35.67	105.05
12	70	230	0.30	300	27.22	117.58
13	70	210	0.45	300	12.17	67.39
14	70	210	0.45	300	12.65	64.67
15	70	190	0.30	300	9.24	54.02
16	70	210	0.60	100	9.61	53.02
17	50	210	0.45	300	11.45	50.44
18	70	210	0.60	300	9.71	59.67
19	70	190	0.45	500	11.93	35.10
20	90	210	0.45	300	30.00	100.79
21	90	210	0.60	300	26.16	80.49

22	70	210	0.45	100	11.93	64.59
23	90	190	0.45	300	23.38	82.20
24	70	210	0.30	500	15.53	67.73
25	90	210	0.45	500	29.59	101.59
26	70	230	0.45	300	25.65	93.89
27	70	210	0.30	300	14.09	94.70
28	70	190	0.60	300	1.10	16.75
29	70	190	0.45	300	8.45	49.54
30	50	190	0.45	300	1.83	14.39
31	50	210	0.60	300	1.85	40.81
32	70	210	0.45	300	12.61	70.09
33	50	210	0.45	300	11.82	48.79
34	70	210	0.30	100	15.79	72.38
35	70	210	0.45	500	13.44	62.53
36	50	210	0.30	300	13.86	52.02
37	90	210	0.30	300	39.21	120.35
38	50	210	0.45	100	9.94	58.98
39	70	210	0.45	100	12.06	65.23

219

220   In order to show clearly the variation trends of the Inter-Strength and Intra-

221 Strength of printed parts as a function of printing parameters, experimental results are

222 presented in Fig. 3. Note that for BBD, only tests in the center points were designed to

223 repeat for evaluating the error of experiments, therefore only these results had error

224   bars. In Fig. 3 (a), it can be found that when the printing temperature was 190 °C, Inter-

225   Strength increased with the increase of printing speed. However, when printing

226   temperature was 210 °C and 230 °C, it seemed that printing speed had an insignificant

227   effect on the Inter-Strength of CRFRPP. Similarly, the change of Intra-Strength as a

228   function of printing speed also presented different trends under different printing

229   temperatures. In Fig. 3 (b), it can be seen that when printing temperature and printing

230   speed were at their center level, the Inter-Strength and Intra-Strength of CRFRPP under

231   three extrusion flow rates decreased with the increase of layer thickness and the degree

232   of decline was different under different extrusion flow. The interactions between

233   printing parameters were obvious and discrete experimental results showed nonlinear

234   and complex rules. Therefore, they were combined with the prediction models to know

235   the overall rules, which were necessary for the optimization.

236
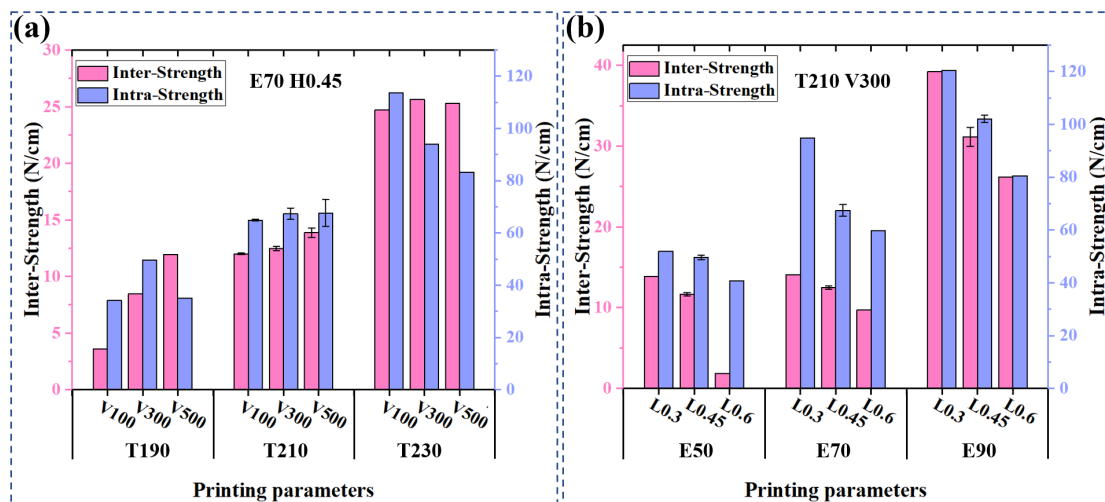
238   **Fig. 3.** Inter-Strength and Intra-Strength of the CRFRPP under different printing

239   parameters.

240

3.2 Evaluation results of models

Fig. 4 shows the R^2 score and error (MAE, RMSE, MedAE) of the prediction models for Inter-Strength and Intra-Strength. In Fig. 4 (a), it can be seen that all three prediction models for Inter-Strength showed higher R^2 scores. However, for Intra-Strength, RSM presented a relatively lower R^2 score. In addition, ANOVA results (see in Tables S1 and S2 in the Supplementary material) found that for both Inter-Strength and Intra-Strength, the Lack of Fit of RSM was significant, which meant the fit of RSM to actual results was significantly inaccurate. Besides, RF presented an acceptable R^2 score (above 0.9) and ANN showed the highest R^2 score as expected. In addition, the R^2 score on the training dataset and test dataset were also calculated to evaluate whether the ANN model was over-fitting. If the model presented a high R^2 score on the training dataset but a low R^2 score in the test dataset, it meant that overfitting occurred during the training process, indicating poor generalizability of the models. In this study, for Inter-Strength, the R^2 of ANN model on the training and test dataset were 0.9682 and 0.9677, respectively. And for Intra-Strength, the R^2 of ANN model on the training and test dataset were 0.9449 and 0.9513, respectively. It was found that the R^2 of the ANN model on the training set was not significantly bigger than that on the test set. Therefore, there seemed to be no obvious overfitting phenomenon in this work.

The R^2 score is an intuitive way to evaluate the performance of each model on the dataset, but it cannot directly quantify the error for specific data. To directly measure

16

261   the practicality of the model for the problem, errors between predicted values and actual

262   values were also used for model evaluation, as shown in Fig. 4 (b). It can be found that

263   among the three models, ANN had the lowest errors for both Inter-Strength and Intra-

264   Strength predictions.

265
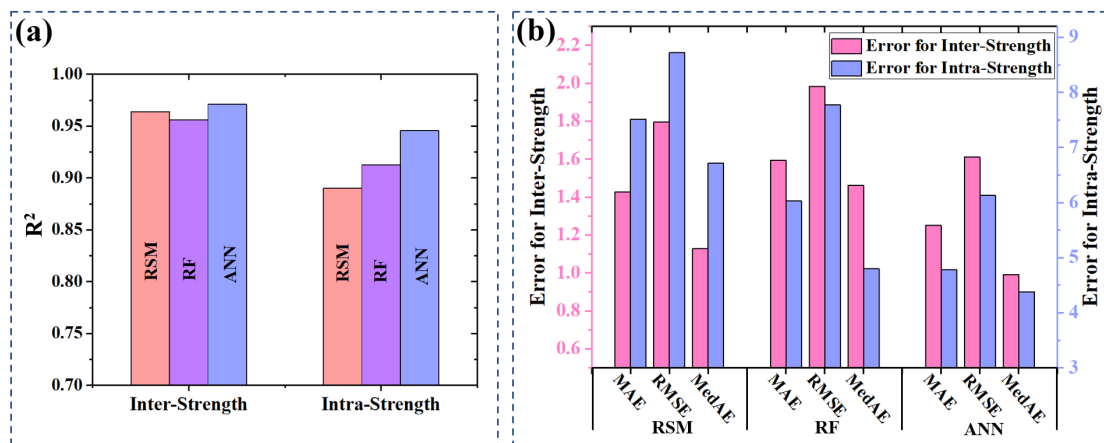
266

267   **Fig. 4.** (a) R^2 score and (b) errors (MAE, RMSE, MedAE) of the prediction models

268   for Inter-Strength and Intra-Strength.

269

270   **3.3 Predicted results**

271   Fig. 5 presents the ANN prediction results because ANN prediction results had the

272   highest accuracy. Note that the step sizes of the printing parameters for the predicting

273   dataset were: E: 5%, T: 5 °C, L: 0.05 mm, and V: 50 mm/min. Only part of the results

274   was shown here as they were sufficient to show the major effects of printing parameters

275   on Inter-Strength and Intra-Strength of CRFRPP. In Fig. 5 (a), it can be found that when

276   layer thickness and printing speed were at their center level, the Inter-Strength of

17

277   CRFRPP increased with the increase of extrusion flow rate and printing temperature

278   (Similar trends can be found when the layer thickness and printing speed in their other

279   levels). In addition, when the extrusion flow rate was low, as increasing printing

280   temperature, the Inter-Strength of CRFRPP was significantly improved. However,

281   when the extrusion flow rate was high, CRFRPP with moderate printing temperature

282   also had high Inter-Strength. In Fig.5 (b), it can be found that when printing temperature

283   and printing speed were at their center level, the Inter-Strength of CRFRPP decreased

284   with the increase of layer thickness. In addition, when the extrusion flow rate was low,

285   with increasing layer thickness, the Inter-Strength of CRFRPP significantly decreased.

286   However, when the extrusion flow rate was high, CRFRPP with relatively high layer

287   thickness also had high Inter-strength. Intra-Strength presented similar trends as

288   mentioned above under the same printing temperature so they were not shown here. In

289   Fig. 5 (c), it can be seen that when extrusion flow rate and layer thickness were at their

290   center level, printing speed had an insignificant influence on the Inter-Strength of

291   CRFRPP. However, at high printing temperature, the Intra-Strength of CRFRPP

292   decreased with the increase of printing speed as shown in Fig. 5 (d). The above results

293   indicated that good interfacial performance of CRFRPP could be achieved without

294   having to set each print parameter to its highest or lowest value, providing the

295   possibility of multi-objective optimization.

296
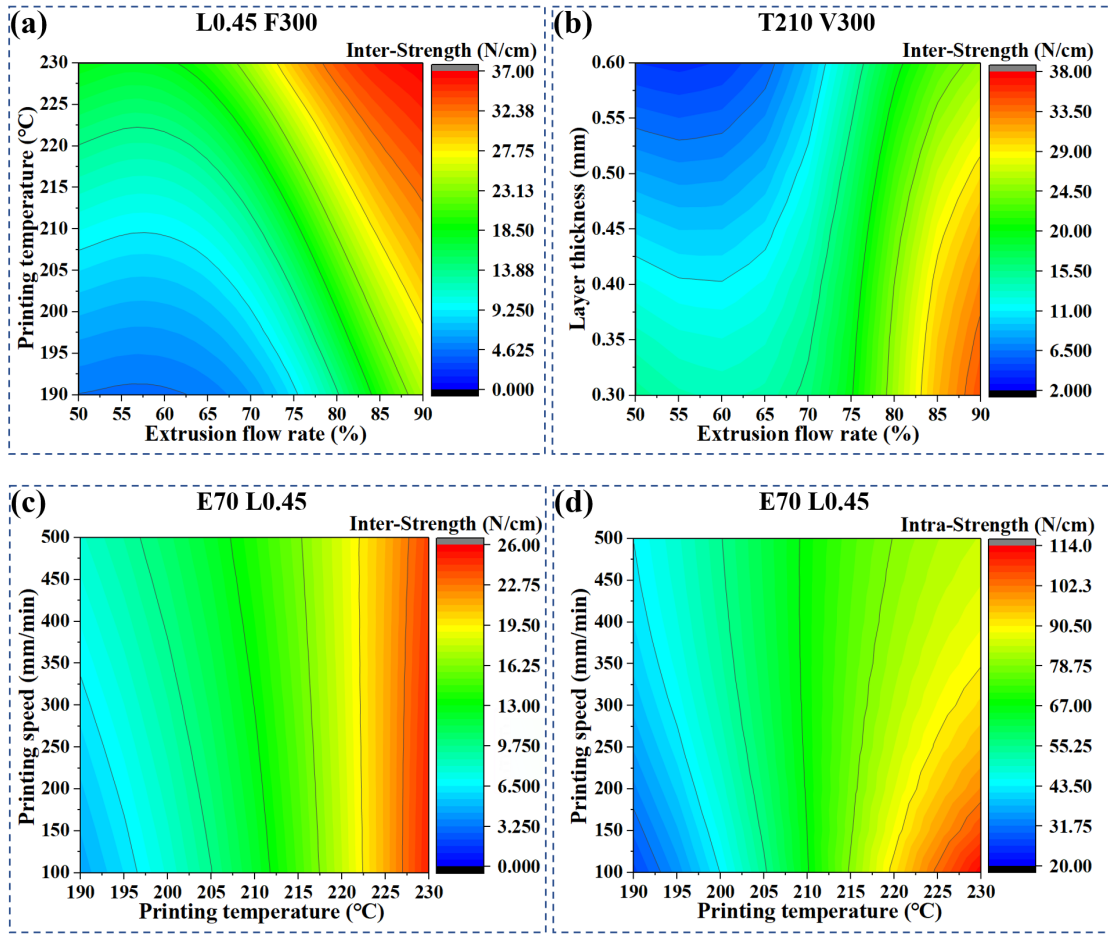
Fig. 5. Inter-Strength and Intra-Strength of CRFRPP under different printing parameters.

3.4 Parameter optimization results

To ensure the high Inter-Strength and Intra-Strength of CRFRPP and improve forming efficiency, based on the ANN prediction results, printing parameters were optimized according to the following principles:

(1) Good Inter-Strength and Intra-Strength of CRFRPP: through adjusting printing parameters, the Inter-Strength and Intra-Strength of CRFRPP could be set as a percentage of their maximum value (in their prediction results range), or as a

19

309　　　　　multiple of the mean or median, depending on practical needs.

310　　　　(2) Low forming time: on the basis of satisfying the first principle, the printing

311　　　　　　parameters that led to the least forming time should be selected. In this study,

312　　　　　　the forming time of printed specimens was given by the slicing software and

313　　　　　　was related to the printing speed and layer thickness.

314　　　　(3) Low energy cost: after satisfying the above two principles, if the available

315　　　　　　parameters were not a unique combination, then a set of parameters with

316　　　　　　relatively low printing temperatures should be selected to save energy.

317　　　　For example, to print 50 mm × 50 mm × 50 mm solid cube specimen (printed parts

318　　with other sizes and shapes also could be chosen according to actual needs), if both

319　　Inter-Strength and Intra-Strength of CRFRPP were set above 95%, 90%, 85%, 80%,

320　　75% and 70% of their maximum values (these thresholds were denoted as Td), the

321　　optimized parameters were listed in Table 4.

322

323　　　　**Table 4.** Optimized parameters for different setting percentages (Td) of their

324　　　　　　　maximum values of Inter-Strength and Intra-Strength.

Td (%)	E (%)	T (°C)	L (mm)	V (mm/min)	Inter-Strength (N/cm)	Intra-Strength (N/cm)	Forming time (h)
95	90	225	0.30	150	38.23	136.84	45.37
90	90	220	0.30	250	37.32	129.63	27.18

|							
85	90	215	0.30	400	36.43	122.19	17.22
80	90	215	0.35	450	35.97	113.93	13.28
75	90	215	0.40	450	35.19	107.66	11.65
70	90	210	0.45	500	33.13	99.71	9.45

4 Discussion

4.1 Comparison of models

As the results discussed in Fig.3 and Fig.5, the variation of Intra-Strength as a function of printing parameters showed more nonlinear and complex rules than those of Inter-Strength, which would be a possible reason that all three Intra-Strength prediction models presented a relatively low R^2 score. As a multiple regression method, RSM can give linear or non-linear models, and each model was scored for accuracy. Eq. (1) and (2) are the highest-scoring models from RSM. In Eq. (1), it can be seen that the model for Inter-Strength prediction is a nonlinear regression equation considering the interaction between parameters, whereas the model for Intra-Strength prediction in Eq. (2) failed to achieve the nonlinear and interactive interactions between parameters. This may be the reason why RSM performs poorly in Intra-Strength prediction.

$$Inter - Strength = 108.84955 - 1.24548E - 1.14408T - 23.56785L +$$
$$0.11136V - 0.002522E * T - 0.086167E * L - 0.000148E * V + 0.117417T * L -$$
$$0.000484T * V + 0.002750L * V + 0.016940E * E + 0.004365T * T -$$
$$25.245647L * L + 7.217331V * V \tag{1}$$

342    $\mathrm{Intra - Strength} = -261.44119 + 1.34246E + 1.336071T - 86.82048L -$

343    $0.01282V$ (2)

344   Fig. 6 shows the schematic graph of the structure of the ANN prediction model for

345   Intra-Strength in this work. The ANN structure in this study comprises one input layer,

346   two hidden layers and one output layer, and each layer contains some neurons. Neurons

347   in two neighboring layers are linked, and the magnitudes of the links between neurons

348   in two adjacent layers are referred as "weight" [47]. The difference between the

349   expected and true output values was utilized to change the weight for increasing

350   accuracy. The error usually gets smaller after a few iterations. As a result, ANN could

351   capture the complicated and nonlinear relationship between the parameters and Intra-

352   Strength, which was the reason why ANN had the best performance for Intra-Strength

353   prediction.

354
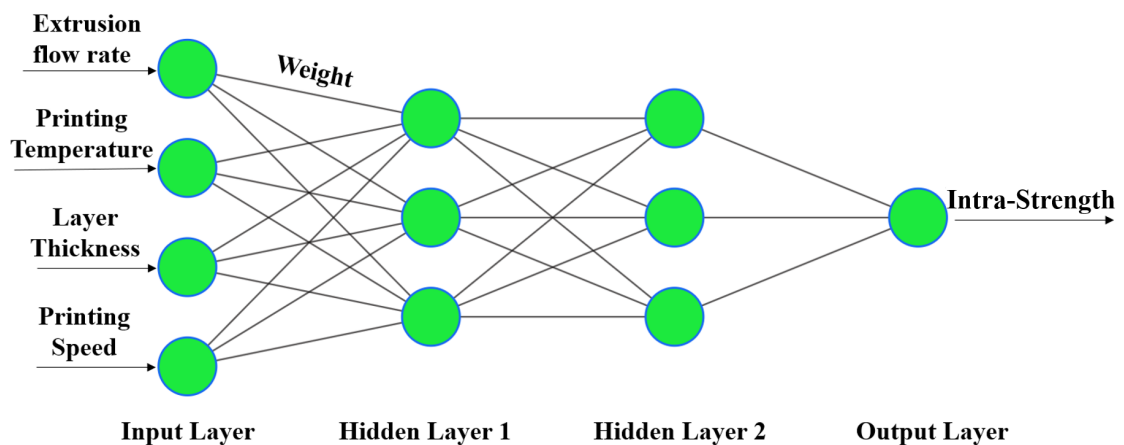
356   **Fig. 6.** Schematic graph of the structure of ANN prediction model for Intra-Strength.

357

358   Although RF did not perform as well as ANN, it also gave an acceptable R^2 score

359   (above 0.9). Moreover, its main advantage is that it can output the importance of

360   parameters, which can evaluate what extent a given printing parameter influences the

361   Inter-Strength and Intra-Strength from a holistic point of view. The importance of

362   parameters will be discussed in detail in the next section.

363   **4.2 Effects of printing parameter on the interfacial properties**

364   Fig.7 shows the importance of four printing parameters. It can be found that

365   extrusion flow rate (E) had the most important influence on both Inter-Strength and

366   Intra-Strength. And printing speed (V) had a relatively small influence on both Inter-

367   Strength and Intra-Strength. For Intra-Strength, printing temperature had close

368   importance compared to extrusion flow rate. One parameter with higher importance

369   should be considered firstly in the adjustment to obtain better properties. For example,

370   in this study, to obtain higher Inter-Strength and Intra-Strength, the first and most

371   important thing is to select the appropriate extrusion flow rate, followed by adjusting

372   the printing temperature and layer thickness, and finally to consider adjusting the

373   printing speed. In addition, one parameter with higher importance indicated it has a

374   relatively narrow parameter selection window. For example, as the optimized results in

375   Table 4, when Inter-Strength and Intra-Strength of CRFRPP were set above from 95%

376   to 70% of their maximum value, all optimized extrusion flow rates were 90%.

377
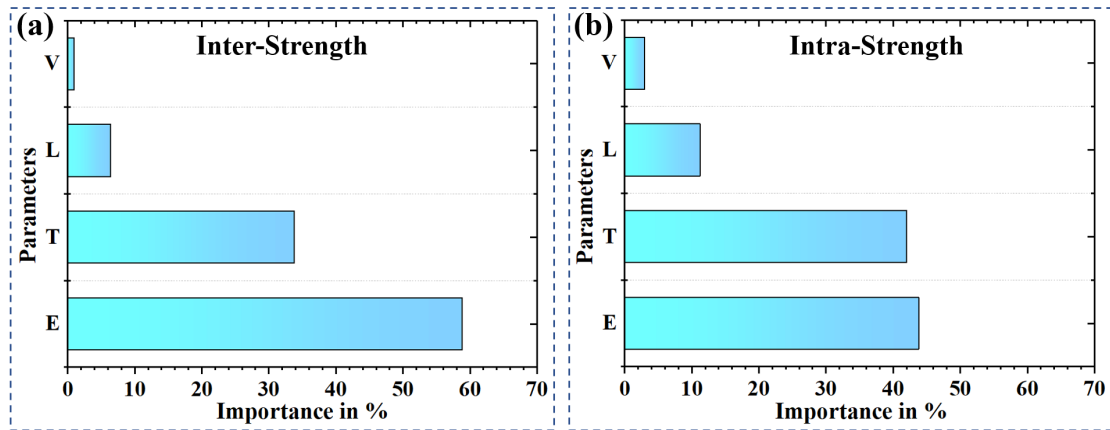
378

379 **Fig. 7.** The importance of four printing parameters, which can evaluate to what extent

380   a given printing parameter influences the Inter-Strength and Intra-Strength from a

381   holistic point of view.

382

383   Fig. 8 shows the typical fracture surfaces of CRFRPP after Inter-Strength and

384 Intra-Strength tests. In Fig. 8 (a), it can be found that interlayer debonding contained

385 fiber/matrix debonding (as shown in area 1) and matrix/matrix debonding (as shown in

386 area 2). In Fig. 8 (b), the debonding between the fine ramie fiber branches of yarns and

387 resin (as shown in area 3) and debonding between resin and resin can be seen (as shown

388 in area 4). Therefore, both the adhesion strength of interlayer resin and the degree of

389 impregnation of fiber had important influence on the interlayer interaction.
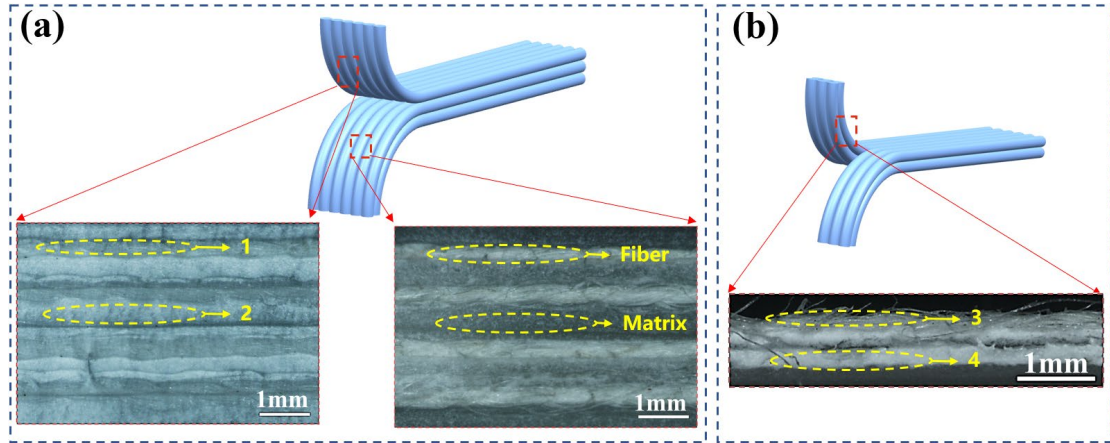
Fig. 8. Typical fracture surfaces of CRFRPP after (a) Inter-Strength and (b) Intra-Strength tests, in which, area 1 is fiber/matrix debonding, area 2 is matrix/matrix debonding, area 3 is the debonding between the fine ramie fiber branches of yarns and resin and area 4 is debonding between resin and resin.

Fig. 9 shows the fracture surfaces of CRFRPP under different printing parameters. Note that the fracture surfaces in which fibers can be seen after Inter-Strength tests (similar to the right image in Fig. 8 (a)) were not presented here because their difference was less visible compared with the fracture surfaces in which fibers were hard to be seen after Inter-Strength tests (just like the left image in Fig. 8 (a)). The interface morphologies at different printing speeds showed limited differences and therefore were not presented here. As shown in Fig. 9 (a) and (g), at a given printing temperature of 190 °C, when the extrusion flow rate was low, obvious voids between filaments could be seen. These defects could seriously decrease the Intra-Strength of CRFRPP. As a result, the Intra-Strengths of CRFRPP at lower extrusion flow rates and lower printing

406 temperatures were significantly inferior to those at higher extrusion flow rates and

407 higher printing temperatures (see Figs. 3 and 5). Comparing to Fig. 9 (a) with (c), more

408 and obvious defects can be seen in the fracture surface of CRFRPP with low printing

409 temperature. In Fig. 9 (b), interlayer debonding can be seen in the fracture surface after

410 Intra-Strength tests, indicating the bonding between layers was poor under low

411 extrusion flow rate and low printing temperature. In addition, the fracture surface of

412 CRFRPP with low extrusion flow rate and low printing temperature was smoother. A

413 smooth surface means there are limited plastic deformations during debonding,

414 indicating adhesion strength is poor. Similar results were also reported by Petersmann

415 et al. [39]. Comparing Fig. 9 (e) and (f) to Fig. 9 (k) and (l), it can be found that the

416 fracture surface became smoother as increasing the layer thickness. In addition, obvious

417 interlayer debonding can be seen in the fracture surface after Intra-Strength test (Fig. 9

418 (l)), which indicated the bonding between layers of CRFRPP was very poor at a high

419 layer thickness. As a result, the Inter-Strengths of CRFRPP at higher layer thicknesses,

420 lower extrusion flow rates and lower printing temperatures decreased significantly

421 compared to those at lower layer thicknesses, higher extrusion flow rates and higher

422 printing temperatures (see Figs. 3 and 5).

423
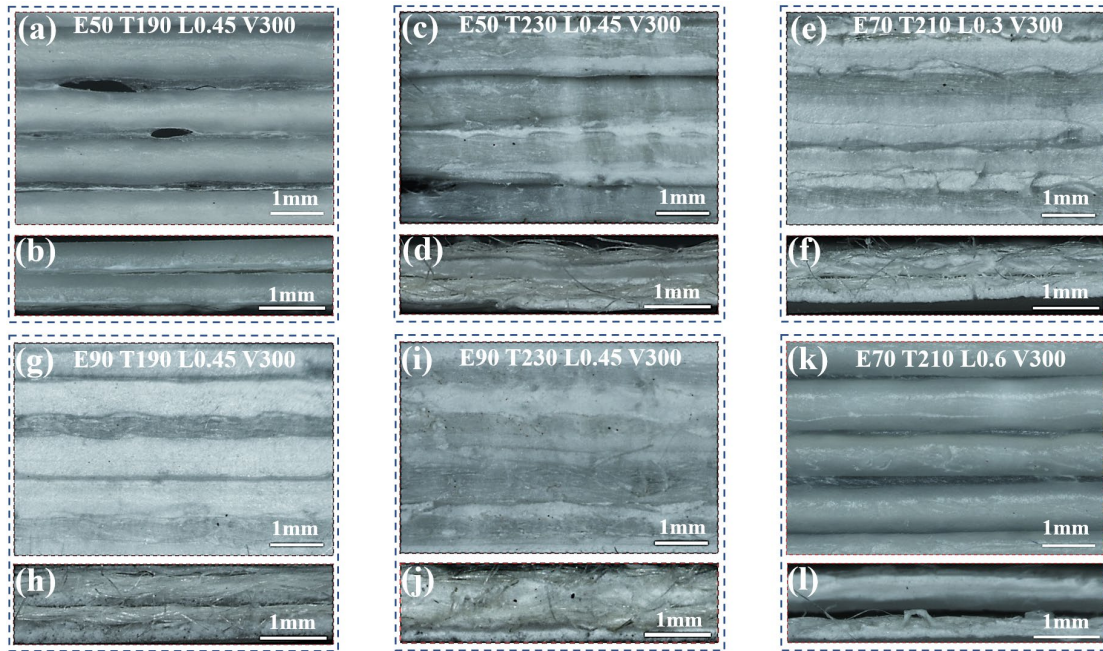
Fig. 9. Fracture surfaces of CRFRPP prepared under different printing parameters.

Factors such as matrix content, temperature and pressure during the forming process could affect the impregnation of fiber by resin and the microstructures such as pores and defects, thus affecting the interface properties of 3D-printed continuous fiber reinforced composites. Printing parameters in this study directly or indirectly affect the above factors and thus affect the Inter-Strength and Intra-Strength of CRFRPP. More specifically, increasing the extrusion flow rate could increase the matrix content, thus could (1) increase the contact pressure between extruded filaments and layers to promote better connections; (2) enable the fiber to be impregnated adequately by the matrix; and (3) enable more matrix flow into interlayer so to reduce the porosity, promoting better interface connection. Increasing the layer thickness could decrease forming pressure, which would increase the interface gap between deposited beams and

438 layers, causing less interface interaction. Similar discussion can be found in Ref. [6].

439 Increasing the printing temperature could increase the fluidity of the matrix, which

440 could (1) enable the matrix better impregnate the fiber; and (2) cause a lower ratio of

441 deposited filament height to width, resulting in a larger contact area between adjacent

442 filament as reported by Ref. [15, 38], causing more interfacial interaction. Vaes et al.

443 [48] reported that as the printing temperatures increase, the interlayer bond strength of

444 3D-printed specimen increased since the weld time between layers increased. At high

445 printing temperatures, the thermoplastic matrix had high fluidity, which made the

446 deposited filaments more susceptible to small perturbation [15]. In addition, high

447 printing speed could cause more perturbation of deposited filaments, which might result

448 in defects between adjacent filaments in a layer. Therefore, the Intra-Strength of

449 CRFRPP with high printing temperature decreased with the increase of printing speed

450 (Fig.5 (d)).

451 **4.3 Parameter optimization**

452 As shown in Table 4, compared to CRFRPP with optimized parameters when Td

453 was set at 90%, Inter-Strength and Intra-Strength of CRFRPP with optimized

454 parameters when Td was set at 80% decreased by 4% and 12%, respectively. However,

455 its forming speed improved by 105%. It can be seen that after parameter optimization,

456 the strength was not reduced much while the forming efficiency was greatly improved.

457 Therefore, in the actual production process, the optimization threshold can be set

458 according to the actual needs, and then the parameters can be optimized based on the

459   prediction results to ensure the strength of printed parts while improving the production

460   efficiency and reducing costs. This could boost the wide application of 3D printing

461   technology.

462   **4.4 Interfacial properties and mechanical performance**

463   To investigate how the difference in interfacial properties can be translated to the

464   mechanical performance, bending tests were performed on printed specimens in

465   directions perpendicular to the layers (out-of-plane) and parallel to the layers (in-plane).

466   Fig. 10 shows the in-plane and out-of-plane flexural modulus and flexural strength of

467   CRFRPP under different printing parameters. Note that the flexural properties at

468   different printing speeds were not shown here because printing speed had insignificant

469   effects on interfacial properties as stated above. And note that unmarked printing

470   parameters are in the middle values in our study range. In Fig. 10, it seemed that the

471   out-of-plane and in-plane flexural strength and modulus of the specimen did not present

472   significant difference, which may be caused by a variety of reasons. This section

473   focused on how the difference in interfacial properties influenced the mechanical

474   performance, so the insignificant difference between the out-of-plane and in-plane

475   flexural mechanical properties of the specimen was not discussed in detail. In addition,

476   combining the results shown in Fig. 10 with those presented in Figs. 3 and 5, it could

477   be found poor interface strengths resulted in inferior flexural properties.

478
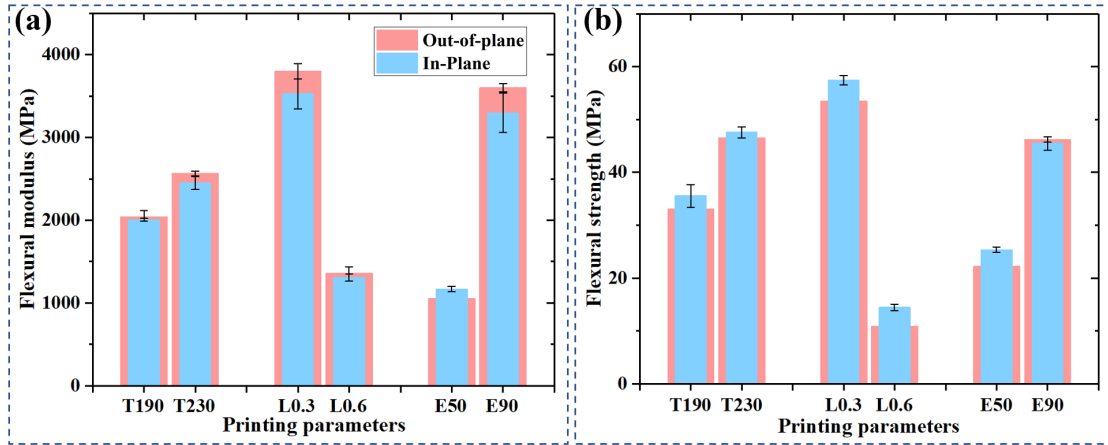
**Fig. 10.** (a) Flexural modulus and (b) flexural strength of CRFRPP under different printing parameters.

In order to further explore how interfacial properties affect flexural mechanical properties of CRFRPP, the typical failure modes of specimens in bending tests are shown in Fig. 11. Note that only the failure behaviors of specimens with printing temperatures of 190 °C and 230 °C were shown here. For specimens with layer thickness of 0.6 mm and with extrusion flow rate of 50%, the failure behaviors were similar to the failure modes of specimens with printing temperatures of 190 °C. For specimens with layer thickness of 0.3 mm and with extrusion flow rate of 90%, the failure behaviors were similar to the failure modes of specimens with printing temperatures of 230 °C, thus they were not shown here. In Fig. 11, it was observed that the specimen printed at 190 °C (which exhibited poor interfacial strengths) showed significant interlayer delamination during out-of-plane bending loading (see Fig. 11(a)). In contrast, the specimen printed at 230 °C did not present delamination during the

495   bending test, and their failure mode was the breakages of the fiber and matrix (see Figs.

496   11(b) and (d)). In addition, delamination was not seen on the front view of the specimen

497   printed at 190 °C when subjected to in-plane bending load (see Fig. 11(c)). However,

498   from the top view, the specimen printed at 190 °C exhibited significant interlayer

499   delamination when subjected to in-plane bending load (see Fig. 11(e)). From the above

500   results, it could be found that printed specimens with weak interfacial strength suffered

501   interlaminar delamination failure when subjected to either in-plane or out-of-plane

502   bending loads, leading to the ineffective load-bearing capacity of the fibers and matrix,

503   thus greatly weakening the mechanical properties of the composites. In addition,

504   delamination of adjacent printed filaments within a layer was not found when subjected

505   to bending loads, which was because of the much higher Intra-Strength than Inter-

506   Strength for printed samples with the same printing parameters (see Figs. 3 and 5).

507

508
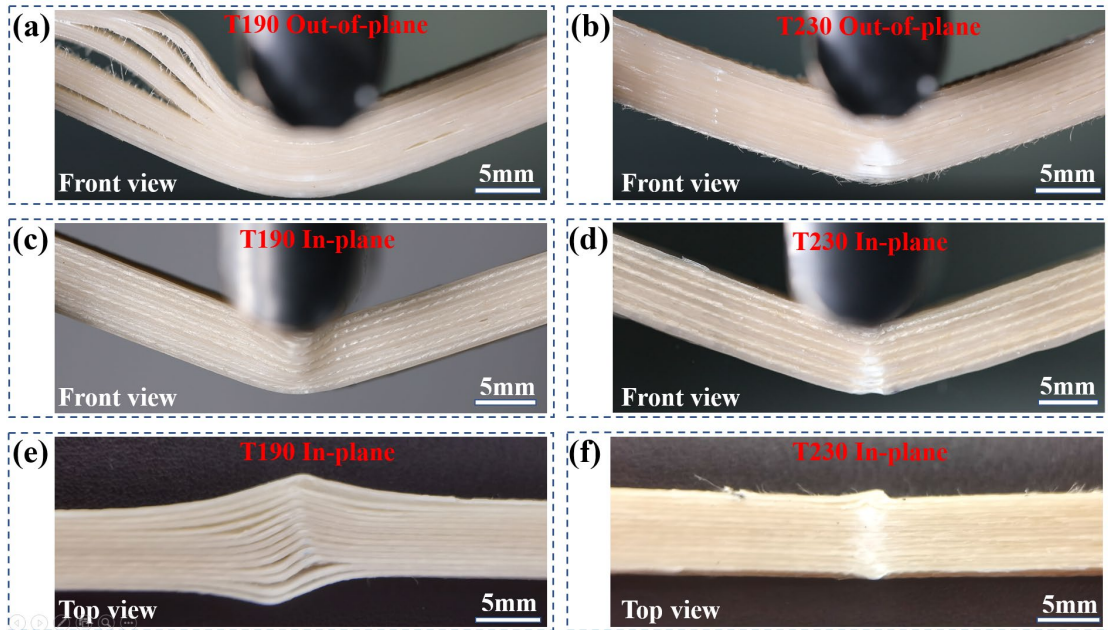
509

510 **Fig. 11.** Failure modes of specimens in bending tests under different printing

511 parameters.

512

513 **5 Conclusion**

514   In this study, the Inter-Strength and Intra-Strength of CRFRPP under different

515 printing parameters were predicted by RSM and two ML methods: RF and ANN, based

516 on the experimental data. Among the three methods, ANN showed the highest

517 prediction accuracy, whereas RF presented acceptable accuracy while providing the

518 importance of the parameters. The result of the importance of the parameters showed

519 that extrusion flow rate had the most important influence on both Inter-Strength and

520 Intra-Strength and printing speed presented a relatively small effect on the above two

521 properties. More specifically, higher extrusion flow rates, lower layer thicknesses, and

522 higher printing temperatures led to higher Inter-Strength and Intra-Strength of CRFRPP.

523   Moreover, the printing parameters were optimized based on the prediction. The

524   optimization results suggested that the forming efficiency could increase significantly

525   while the Inter-Strength and Intra-Strength of CRFRPP were not affected significantly.

526   Therefore, based on the prediction results, the production efficiency of 3D-printed

527   components could be improved using the proposed parameter optimization procedure

528   and ensuring the properties, boosting the industrial application of 3D-printed products.

529   Furthermore, the bending tests were carried out to investigate the effects of interfacial

530   properties on the mechanical performance. The results found that printed specimens

531   with weak interfacial strength suffered interlaminar delamination failure during

532   bending loading, which greatly weakened the mechanical properties of the CRFRPP.

533   In future work, the effects of more printing parameters (e.g., platform temperature

534   and print line spacing) and even environmental parameters (e.g., temperature and

535   humidity of the printing chamber) on interfacial properties will be considered to study

536   for achieving more precise and stable analysis results. In addition, more data

537   preprocessing methods, training and test dataset preparation approaches and more ML

538   methods will be attempted to establish more robust and more applicable models.

539   Furthermore, material modification for increasing the interfacial reaction between the

540   fiber and matrix using maleic anhydride grafted polypropylene and sodium hydroxide

541   will be systematically studied.

546

547 **References**

548 [1] S.A.M. Tofail, E.P. Koumoulos, A. Bandyopadhyay, S. Bose, L. O'Donoghue, C.

549 Charitidis, Additive manufacturing: scientific and technological challenges, market

550 uptake and opportunities, Mater. Today 21(1) (2018) 22-37.

551 [2] X. Wang, M. Jiang, Z. Zhou, J. Gou, D. Hui, 3D printing of polymer matrix

552 composites: A review and prospective, Composites, Part B 110 (2017) 442-458.

553 [3] P.K. Penumakala, J. Santo, A. Thomas, A critical review on the fused deposition

554 modeling of thermoplastic polymer composites, Composites, Part B (2020) 108336.

555 [4] N. van de Werken, H. Tekinalp, P. Khanbolouki, S. Ozcan, A. Williams, M. Tehrani,

556 Additively manufactured carbon fiber-reinforced composites: State of the art and

557 perspective, Addit. Manuf. 31 (2020) 100962.

558 [5] K. Wang, S. Li, Y. Wu, Y. Rao, Y. Peng, Simultaneous reinforcement of both rigidity

559 and energy absorption of polyamide-based composites with hybrid continuous fibers

560 by 3D printing, Compos. Struct. 267 (2021) 113854.

561 [6] P. Cheng, K. Wang, X. Chen, J. Wang, Y. Peng, S. Ahzi, C. Chen, Interfacial and

562 mechanical properties of continuous ramie fiber reinforced biocomposites fabricated

563 by in-situ impregnated 3D printing, Ind. Crops Prod. 170 (2021) 113760.

564 [7] G.D. Goh, Y.L. Yap, S. Agarwala, W.Y. Yeong, Recent progress in additive

565 manufacturing of fiber reinforced polymer composite, Adv. Mater. Technol. 4(1) (2019)

566 1800271.

567 [8] H.J. Aida, R. Nadlene, M.T. Mastura, L. Yusriah, D. Sivakumar, R.A. Ilyas, Natural

568 fibre filament for Fused Deposition Modelling (FDM): a review, Int. J. Sustainable Eng.

569 14(6) (2021) 1988-2008.

570   [9] A. Pappu, K.L. Pickering, V.K. Thakur, Manufacturing and characterization of

571   sustainable hybrid composites using sisal and hemp fibres as reinforcement of poly

572   (lactic acid) via injection moulding, Ind. Crops Prod. 137 (2019) 260-269.

573   [10] R. Matsuzaki, M. Ueda, M. Namiki, T.-K. Jeong, H. Asahara, K. Horiguchi, T.

574   Nakamura, A. Todoroki, Y. Hirano, Three-dimensional printing of continuous-fiber

575   composites by in-nozzle impregnation, Sci. Rep. 6(1) (2016) 23058.

576   [11] A. Le Duigou, A. Barbé, E. Guillou, M. Castro, 3D printing of continuous flax

577   fibre reinforced biocomposites for structural applications, Mater. Des. 180 (2019)

578   107884.

579   [12] A. Le Duigou, G. Chabaud, R. Matsuzaki, M. Castro, Tailoring the mechanical

580   properties of 3D-printed continuous flax/PLA biocomposites by controlling the slicing

581   parameters, Composites, Part B 203 (2020) 108474.

582   [13] F.-L. Jin, R.-R. Hu, S.-J. Park, Improvement of thermal behaviors of biodegradable

583   poly(lactic acid) polymer: A review, Composites, Part B 164 (2019) 287-296.

584   [14] X. Wang, S. Peng, H. Chen, X. Yu, X. Zhao, Mechanical properties, rheological

585   behaviors, and phase morphologies of high-toughness PLA/PBAT blends by in-situ

586   reactive compatibilization, Composites, Part B 173 (2019) 107028.

587   [15] K. Wang, R. Cai, Z. Zhang, J. Liu, S. Ahzi, Y. Peng, Y. Rao, Compressive behaviors

588   of 3D printed polypropylene-based composites at low and high strain rates, Polym. Test.

589   103 (2021) 107321.

590   [16] M. Spoerk, F. Arbeiter, I. Ragv~, C. Holzer, J. Gonzalez-Gutierrez, Mechanical

591   Recyclability of Polypropylene Composites Produced by Material Extrusion-Based

592   Additive Manufacturing, Polymers 11 (2019).

593   [17] B.A. Moore, E. Rougier, D. O'Malley, G. Srinivasan, A. Hunter, H. Viswanathan,

594   Predictive modeling of dynamic fracture growth in brittle materials with machine

595   learning, Comput. Mater. Sci. 148 (2018) 46-53.

596   [18] I. Kalogeris, Advanced surrogate modeling and machine learning methods in

597   computational stochastic mechanics, (2020).

598   [19] F. Wang, J. Wu, L. Hu, C. Yu, B. Wang, X. Huang, K. Miller, A. Wittek, Evaluation

599   of the head protection effectiveness of cyclist helmets using full-scale computational

600   biomechanics modelling of cycling accidents, J. Saf. Res. 80 (2022) 109-134.

601   [20] R. Cai, K. Wang, W. Wen, Y. Peng, M. Baniassadi, S. Ahzi, Application of machine

602   learning methods on dynamic strength analysis for additive manufactured

603   polypropylene-based composites, Polym. Test. (2022) 107580.

604   [21] N. Wei, S. Yao, Y. Rao, K. Wang, Y. Peng, An integrated prediction model for

605   processing related yield strength of extrusion-based additive manufactured polymers,

606   Mech. Adv. Mater. Struct. (2022) 1-11.

607   [22] A.K. Sood, R.K. Ohdar, S.S. Mahapatra, Experimental investigation and empirical

608   modelling of FDM process for compressive strength improvement, J. Adv. Res. 3(1)

609   (2012) 81-90.

610   [23] C. Wang, X.P. Tan, S.B. Tor, C.S. Lim, Machine learning in additive manufacturing:

611   State-of-the-art and perspectives, Addit. Manuf. 36 (2020) 101538.

612   [24] O.A. Mohamed, S.H. Masood, J.L. Bhowmik, Investigation of dynamic elastic

613   deformation of parts processed by fused deposition modeling additive manufacturing,

614   Adv. Prod. Eng. Manag. 11(3) (2016) 227-238.

615   [25] Ö. Bayraktar, G. Uzun, R. Çakiroğlu, A. Guldas, Experimental study on the 3D-

616   printed plastic parts and predicting the mechanical properties using artificial neural

617   networks, Polym. Adv. Technol. 28(8) (2017) 1044-1051.

618   [26] A. Douard, C. Grandvallet, F. Pourroy, F. Vignat, An Example of Machine Learning

619   Applied in Additive Manufacturing, 2018 IEEE International Conference on Industrial

620   Engineering and Engineering Management (IEEM), 2018, pp. 1746-1750.

621   [27] K. Aoyagi, H. Wang, H. Sudo, A. Chiba, Simple method to construct process maps

622   for additive manufacturing using a support vector machine, Addit. Manuf. 27 (2019)

623   353-362.

624 [28] S. Wang, Y. Ma, Z. Deng, S. Zhang, J. Cai, Effects of fused deposition modeling

625 process parameters on tensile, dynamic mechanical properties of 3D printed polylactic

626 acid materials, Polym. Test. 86 (2020) 106483.

627 [29] S.M.F. Kabir, K. Mathur, A.-F.M. Seyam, A critical review on 3D printed

628 continuous fiber-reinforced composites: History, mechanism, materials and properties,

629 Compos. Struct. 232 (2020) 111476.

630 [30] M.A. Caminero, J.M. Chacón, I. García-Moreno, J.M. Reverte, Interlaminar

631 bonding performance of 3D printed continuous fibre reinforced thermoplastic

632 composites using fused deposition modelling, Polym. Test. 68 (2018) 415-423.

633 [31] T. Liu, X. Tian, M. Zhang, D. Abliz, D. Li, G. Ziegmann, Interfacial performance

634 and fracture patterns of 3D printed continuous carbon fiber with sizing reinforced PA6

635 composites, Composites, Part A 114 (2018) 368-376.

636 [32] Y. Wu, K. Wang, V. Neto, Y. Peng, R. Valente, S. Ahzi, Interfacial behaviors of

637 continuous carbon fiber reinforced polymers manufactured by fused filament

638 fabrication: A review and prospect, International Journal of Material Forming 15(3)

639 (2022) 18.

640 [33] S. Li, K. Wang, W. Zhu, Y. Peng, S. Ahzi, F. Chinesta, Contributions of interfaces

641 on the mechanical behavior of 3D printed continuous fiber reinforced composites,

642 Constr. Build. Mater 340 (2022) 127842.

643 [34] D. Yavas, Z. Zhang, Q. Liu, D. Wu, Interlaminar shear behavior of continuous and

644 short carbon fiber reinforced polymer composites fabricated by additive manufacturing,

645 Composites, Part B 204 (2021) 108460.

646 [35] S. Beg, S. Akhter, Box–Behnken Designs and Their Applications in

647 Pharmaceutical Product Development, in: S. Beg (Ed.), Design of Experiments for

648 Pharmaceutical Product Development: Volume I : Basics and Fundamental Principles,

649 Springer Singapore, Singapore, 2021, pp. 77-85.

650 [36] S. Zhang, Y. Sun, Y. Cheng, P. Huang, M.O. Oladokun, Z. Lin, Response-surface-

model-based system sizing for Nearly/Net zero energy buildings under uncertainty, Applied Energy 228 (2018) 1020-1031.

[37] X. Shen, G. Zhang, B. Bjerg, Assessments of experimental designs in response surface modelling process: Estimating ventilation rate in naturally ventilated livestock buildings, Energy and Buildings 62 (2013) 570-580.

[38] S. Charlon, J. Le Boterff, J. Soulestin, Fused filament fabrication of polypropylene: Influence of the bead temperature on adhesion and porosity, Addit. Manuf. 38 (2021) 101838.

[39] S. Petersmann, P. Spoerk-Erdely, M. Feuchter, T. Wieme, F. Arbeiter, M. Spoerk, Process-induced morphological features in material extrusion-based additive manufacturing of polypropylene, Additive Manufacturing 35 (2020) 101384.

[40] M.V. Candal, I. Calafel, N. Aranburu, M. Fernández, G. Gerrica-Echevarria, A. Santamaría, A.J. Müller, Thermo-rheological effects on successful 3D printing of biodegradable polyesters, Addit. Manuf. 36 (2020) 101408.

[41] M.V. Candal, I. Calafel, M. Fernández, N. Aranburu, R.H. Aguirresarobe, G. Gerrica-Echevarria, A. Santamaría, A.J. Müller, Study of the interlayer adhesion and warping during material extrusion-based additive manufacturing of a carbon nanotube/biobased thermoplastic polyurethane nanocomposite, Polymer 224 (2021) 123734.

[42] C.S. Davis, K.E. Hillgartner, S.H. Han, J.E. Seppala, Mechanical strength of welding zones produced by polymer extrusion additive manufacturing, Addit. Manuf. 16 (2017) 162-166.

[43] J.E. Seppala, S. Hoon Han, K.E. Hillgartner, C.S. Davis, K.B. Migler, Weld formation during material extrusion additive manufacturing, Soft Matter 13(38) (2017) 6761-6769.

[44] E. Barocio, B. Brenken, A. Favaloro, R.B. Pipes, Interlayer fusion bonding of semi-crystalline polymer composites in extrusion deposition additive manufacturing,

678 Compos. Sci. Technol. (2022) 109334.

679 [45] F. Pedregosa, G. Varoquaux, A. Gramfort, V. Michel, B. Thirion, O. Grisel, M.

680 Blondel, P. Prettenhofer, R. Weiss, V. Dubourg, Scikit-learn: Machine learning in

681 Python, J. Mach. Learn. Res 12 (2011) 2825-2830.

682 [46] M.A. Mahmood, A.I. Visan, C. Ristoscu, I.N. Mihailescu, Artificial Neural

683 Network Algorithms for 3D Printing, Materials 14(1) (2021) 163.

684 [47] Z. Zhang, Artificial neural network, Multivariate time series analysis in climate

685 and environmental research, Springer2018, pp. 1-35.

686 [48] D. Vaes, M. Coppens, B. Goderis, W. Zoetelief, P. Van Puyvelde, The Extent of

687 Interlayer Bond Strength during Fused Filament Fabrication of Nylon Copolymers: An

688 Interplay between Thermal History and Crystalline Morphology, Polymers 13(16)

689 (2021) 2677.